Hindawi
Shock and Vibration
Volume 2022, Article ID 2090470, 17 pages
https://doi.org/10.1155/2022/2090470

*Research Article*

# A Fluid-Structure Interaction Model for Bridge Safety Assessment under Scour Conditions

**Tzu-Kang Lin, Po-Wei Chen, and Hao-Tun Chang**

*Department of Civil Engineering, National Yang Ming Chiao Tung University, Taipei 30012, Taiwan*

Correspondence should be addressed to Tzu-Kang Lin; tklin@nctu.edu.tw

Received 2 May 2022; Revised 25 June 2022; Accepted 14 July 2022; Published 18 August 2022

Academic Editor: Mahmoud Bayat



Bridge pier scour engendered by typhoons or flooding poses a threat to the stability, bearing capacity, and other performance parameters of bridge foundations. In traditional static evaluation procedures, linear force distributions are used to express the fluid behavior under current forces, which results in overestimation of stability. A finite element simulation was conducted in this study to correctly evaluate the effect of fluid by developing a fluid-solid interaction (FSI) system. In the FSI system, simulation results for both the fluid and solid systems were exchanged. Thus, the force generated by the fluid system could be incorporated into the solid system to estimate the dynamic response of a pier. A scaled single-pier scour test was first conducted numerically and experimentally. The results showed that the established FSI system can consider the fluid-solid interaction and reflect pier scour behavior accurately. To test the validity of the proposed system, the scour process was numerically conducted on an engineering bridge. Two safety factors were proposed to evaluate the stability of the bridge structure under extreme events such as rainfall or typhoon. The result has proven that the scour stability of the bridge pier can be appropriately evaluated by the proposed system.

## 1. Introduction

A survey conducted in the United States indicated that approximately 60% of bridge failures are attributed to hydraulic activity and that only 3% of such failures are attributed to seismic activity [1]. Scour, classified as a hydraulic activity in the survey, is caused by the loss of bed material near the piers due to the water flow. Bridge stability and scour assessment indicated that scouring of piers in rivers can be classified into three types according to its cause and position: degradational, contraction, and local scour [2]. Degradational scour occurs gradually over time due to floods or some human activities. The occurrence of contraction and local scour is directly related to the bridge structure. The flow velocity near a bridge decreases because of the corresponding abutments and piers, resulting in a contraction scour in the riverbed. Among these three types of scour, local scour results in erosion of bed material near the piers due to the generated vortices and poses the greatest threat to the bridge structure.

The complex flow behavior of water near a pier is typically simplified as a linear force in most of the existing regulations. In practice, because of the flow pattern and vortex around a cylindrical or scoured pier, the fluid behavior can be categorized into several series, including surface roller, downflow, horseshoe vortex, and wake vortex [3], as shown in Figure 1. Brücker [4] collected three-dimensional (3D) vortex features through scanning particle image velocimetry. The vortex field was visualized through continuous 2D velocity data collected from a cylindrical tank using an acoustic Doppler velocity profiler (ADVP), which accurately represented the spanwise flow. Graf et al. [5] observed the 2D behavior of a fluid with distinct angles to the current direction by using an ADVP. The boundary and velocity intensity of the horseshoe vortex were described with 0°, 45°, 90°, 157.5°, and 180° to the current direction. The interaction between the horseshoe vortex, wake vortex, and scour hole indicated that vortices occurred not only at the upstream end for the downflow but also at the downstream end for the changes in the slope of the riverbed. Yulistiyanto et al. [6] defined the 2D horizontal flow through vertical

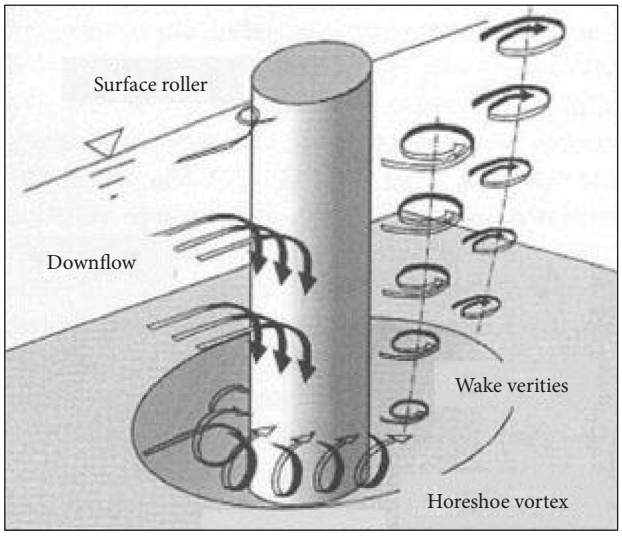


Figure 1: Fluid behavior near the pier with scour [3].

depth integration of continuity and momentum equations. The flow velocity field and water elevation near a cylindrical pier were predicted using the MacCormack method [7]. They indicated that the wake vortices tended to be more unstable and changeable. Experiments indicated similar results with small errors being obtained for wake vortices at the downstream end as the water levels near the surface of the cylindrical piers were underestimated.

Studies have shown the effect of scour on bridge foundation performance such as stability and bearing capacity. Prendergast et al. [8] developed numerical and practical scaled pile models. Analyzing the response of the models after excitation by an impulse force revealed a loss of structural natural frequency and occurrence of scour at the foundation of the piles. A lower dominant frequency was considered to imply a lower constraint, suggesting a weakened structure. Prendergast et al. [9] studied the natural frequency response of structure, and Tseng et al. [10] performed numerical simulations on the piers of offshore wind turbines, concluding that the natural frequency decreased, and the deformation increased with the loss of riverbed materials near the piers.

The flow behavior of water near piers, especially piers with scour, is highly nonlinear, where the velocity fields change with time and distance from the piers. Normally, the effects of fluid behavior may be smaller than those of live and dead loads on a bridge. However, bridge failure may occur because of the overestimation of stability in areas subjected to severe scour. Considering the existing regulations and the complexity of structural design, fluid behavior is typically simplified as a linear distribution in most structural design procedures. Therefore, a method in which both structural and fluid conditions are considered is required to accurately evaluate the stability of bridge structures under the influence of current forces.

An FSI system was conducted in this study to correctly evaluate the effect of fluid-solid interaction. The result of the scaled single-pier scour test showed that the proposed FSI system can consider the nonlinear dynamic interaction and reflect accurate pier scour behavior. Two safety factors were then proposed to evaluate the stability of bridge structure under extreme events. The results can serve as a reference in establishing guidelines for bridge.

The remainder of this study is structured as follows. The methodology, including fluid-solid interaction model, soil model, and short-term Fourier transform, is introduced first. In Section 3, a scour test was conducted using a scaled pier model, and ambient vibration data were collected. Dominant frequencies in the numerical simulation were compared with the experimental frequencies to demonstrate the feasibility of the proposed method. Scour simulation of a practical bridge was developed in Section 4. The structural displacement of the model obtained from a fluid-solid interaction (FSI) simulation was compared with that obtained from a static simulation. To evaluate the stability under serious scour, two safety factors were proposed. The alert and action levels of scour depth at different flow velocities were obtained. Finally, a summary is provided, and conclusions are drawn in Section 5.

## 2. Methodology

To analyze the stability of the bridge by considering the influence of the fluid, two methods, including FSI and Short-Time Fourier Transform (STFT), were applied. These methods are described as follows.

*2.1. Fluid-Solid Interaction Model.* The numerical model consists of a transient structural system and a fluid flow system, where the boundary conditions of these two models are influenced by each other. Thus, by using the fluid-solid interaction model, the response of bridge under the influence of fluid can be simulated. As depicted in Figure 2, the responses of the transient structural and fluid flow modules were connected through system coupling in the simulation. In the solid module, the external force was applied, and the structural displacement was the output. In the fluid module, the geometric shape of the flow field was generated with the structural displacement as the boundary condition, and the fluid behavior was the output. Some important settings for the sophisticated model are listed as follows.

*2.2. Soil Model.* Generally, the soil is compressible and does not have a specific volume, which renders the simulation of Earth pressure in the numerical model difficult. Solid element proposed by Chiroux et al. [11], discrete element method (DEM 1989) proposed by John et al., and the soil spring proposed by Prendergast et al. [8, 11, 12] have been applied to simulate reaction forces in soil. To achieve accurate results, the solid element and DEM require details of the properties of soil. Considering the number of soil parameters required as well as the model complexity, a relatively simplified model, soil spring, was applied in this study. According to the current code in Taiwan [13], the setting of the soil spring in the numerical model is illustrated in Figure 3, and those soil springs set in the structural model can be divided into the following four categories.

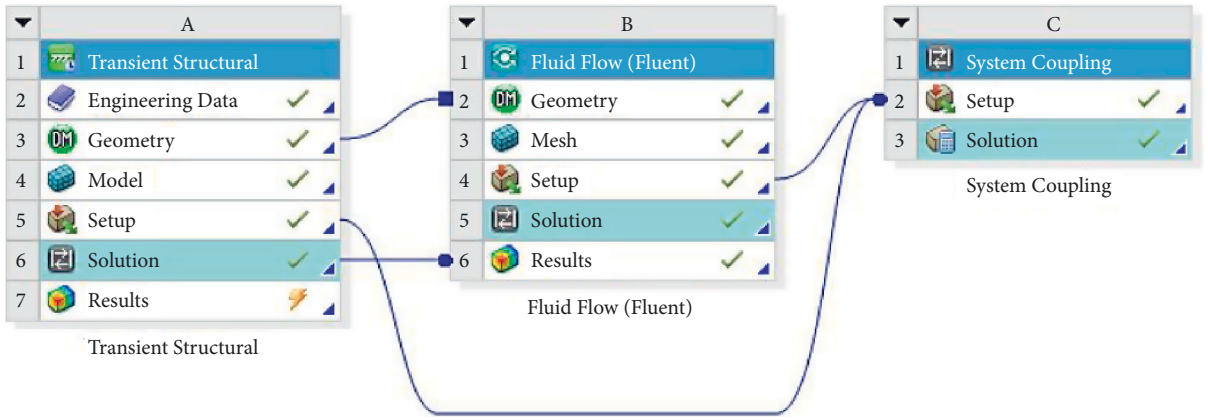


Figure 2: System coupling for FSI simulation.

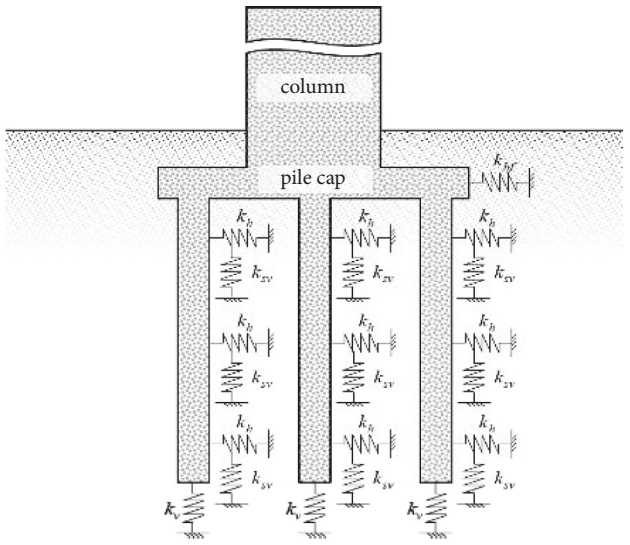


Figure 3: Setting of the soil spring in the numerical model.

*2.2.1. Horizontal Pile Soil Spring.* To simulate the lateral Earth pressure applied to a pile structure when a horizontal external force generates a displacement, the stiffness of the soil springs set horizontally on a pile is expressed as [13]

$$k_h = 0.34(\alpha E_0)^{1.10} D^{-0.31} (EI)^{-0.103}, \quad (1)$$

where $\alpha$ is the modulus of the seismic subgrade reaction and $E_0$ is the modulus of the subgrade deformation. The modulus of the subgrade deformation can be further defined by the $N$ value from the standard penetration test (SPT) as

$$E_0 = 28N, \quad (2)$$

where $D$, $E$, and $I$ are the diameter, Young's modulus, and second axial moment of the area of the pile structure, respectively. For the modulus of the seismic subgrade reaction, $\alpha$ is typically set to 2, considering the seismic event. In this study, the influence of earthquakes was not included; therefore, $\alpha$ was set to 1.

*2.2.2. Vertical Pile Soil Spring.* To simulate the friction between the soil and a pile structure when vertical loading and self-weight are transferred to the foundation by the pier, the stiffness of the soil springs set vertically on the pile can be described as [13]

$$k_{sv} = 0.3k_h, \quad (3)$$

where $k_h$ is the stiffness of the horizontal pile soil spring. As the conditions of friction between soil and the pile surface are unclear and influenced by the construction method and siltation of the riverbed, the friction can be defined according to the reduction of lateral Earth pressure.

*2.2.3. Horizontal Pile Cap Soil Spring.* tTo simulate the lateral Earth pressure applied to the pile cap when a horizontal external force causes structural displacement, the stiffness of soil springs set horizontally on the pile cap can be described as [13]

$$k_{hf} = \frac{(\alpha E_0)}{30}\left(\frac{B_H}{30}\right)^{-3/4}, \quad (4)$$

where $B_H$ is the equivalent foundation width in the direction orthogonal to the horizontal loading. To prevent overestimation of the stiffness of soil in foundation areas characterized by a narrow cross section, the effective width of the foundation $B_H$ should not be greater than the geometric mean of the effective width and effective embedded depth, as described in the following equation:

$$B_H = B_e \left(\leq \sqrt{B_e \cdot L_e}\right), \quad (5)$$

where $B_e$ and $L_e$ are the effective width of the foundation and the effective embedded depth, respectively.

*2.2.4. Vertical Pile Toe Soil Spring.* The reaction force engendered by the soil applied at the bottom of the pile to support the vertical loading and the self-weight transferred from the superstructure can be simulated by the stiffness of the soil springs set vertically on the pile toe as [13]

$$k_v = \frac{(\alpha E_0)}{30}\left(\frac{B_v}{30}\right)^{-3/4}, \quad (6)$$

$$B_v = \sqrt{A_v},$$

where $B_v$ is the equivalent bearing width and $A_v$ is the area that bears the vertical loading.

*2.3. Short-Time Fourier Transform.* Fourier transform is generally applied to discrete signals and can be expressed as

$$X[\omega] = \sum_{n=-\infty}^{\infty} x[n]e^{-i\omega n}, \tag{7}$$

where $n$ is the discrete step in the time domain and $\omega$ is the frequency content after transform. During the scour test, the embedded depth decreased because of the loss of bed elements, leading to a nonconstant model boundary condition. Therefore, Short-Time Fourier Transform (STFT), a method that can be used to analyze the time-frequency domain, was applied and can be expressed as

$$X[m, \omega] = \sum_{n=-\infty}^{\infty} x[n]w[n-m]e^{-i\omega n}, \tag{8}$$

where $n$ represents the time point, $\omega$ represents the frequency, $m$ expresses the time delay, and $w$ is the window function that shifts along the time domain. Changes in modal dynamic features with time can be obtained using the window function. To improve the STFT performance, a Hamming window is adopted as

$$w[n] = 0.53836 - 0.46164\cos\left(\frac{2\pi n}{N-1}\right), \tag{9}$$

where $N$ is the data points of the window length.

## 3. Feasibility Assessment

FSI simulation has been applied in different fields such as pipes [14], turbines [15], hemodynamics [16], aerospace engineering [17], stability of structures [18], numerical method verification [19], flexible cylinder [20], response of submarines [21], vortex vibration [22], liquid storage tanks [23], analysis of cylindrical liquid storage tanks [24], and seismic fragility analysis [25]. As the scour phenomenon is complicated to illustrate, a small-scale scour experiment was conducted to verify the capability of the proposed FSI method, which is designed to simulate the complex interaction between the fluid field, bridge pier, and soil springs.

*3.1. Experiment Setup.* The feasibility assessment was performed by utilizing the dynamic features of the bridge in the frequency domain. The scaled scour model was set in a 37 m × 1 m sink with a depth of 1.2 m, as shown in Figure 4(a). In this scour experiment, a concrete pier structure with a 0.49 m caisson foundation was embedded with a 12 cm initial depth. The length, thickness, and height of the concrete pier are depicted in Figure 4(b). To simulate riverbed erosion, the pump system provided a 10 cm deep water flow with a velocity of 2.5 m/s.

The top of the pier was subjected to vibration, and the spectrum analysis was performed approximately every 5 seconds with a 50% of window overlapping. Scour depth and vibration data were collected using a camera and three velocity meters set on top of the pier model. The location of velocity meters is shown in Figure 5. The ambient vibration in the current direction was applied to calculate the fundamental frequency of the concrete model. In Figure 6, the fundamental frequencies were identified when the embedded depths were 5 cm, 6 cm, and 8 cm, respectively. And these fundamental frequencies were selected as simulation targets. The boundary conditions, including the flow velocity, embedded depth, and water depth of the pier model, are listed in Table 1. The data points of the STFT were selected as 2048 in this study. As the sampling rate was 200 Hz, the window length of 2048 points was about 10 seconds, which fits well with the whole scour duration. Figure 6 presents the STFT results; the orange line represents the embedded depth, and the light-blue line represents the dominant frequency of the pier model. The fundamental frequency decreased with the embedded depth, indicating that the attachment of the pier to the soil became less rigid as the riverbed level decreased.

*3.2. Numerical Simulation.* For an appropriate FSI simulation, the solid and fluid modules are first operated separately with the geometric system linked; the two modules can establish the model that includes a fluid block and piers. The numerical model built in the finite element software is depicted in Figure 7. The model was built according to the same geometric design of the material with Young's modulus of 3 GPa and a density of 103 kg/m$^3$. The solid elements were crashed into numerous small blocks or tetrahedrons. The size of each crashed element around the pile was about 0.2 cm long. As obstacles may lead to extreme flow velocity when the distance between the obstacle and the flow is short, the distance from the edge of the fluid block to the model is set at least 2.5 times the pier diameter, which is 98.4 cm.

The stiffness of soil springs can be obtained from the properties of the soil. To determine the $N$ value of soil without conducting the SPT, the repose angle of soil was measured and used for $N$ value estimation according to Table 2. The measured slope angle was 34.5°, with the corresponding $N$ value ranging from 10 to 30. The $N$ value was tuned according to the experimental data and simulation results. Soil springs, including the horizontal vertical pile soil springs and the vertical pile toe soil spring, were set on the left and right sections of the pile and at the upstream and downstream ends around the pile at a distance of 1 cm throughout the soil layer, respectively. A nonlinear flow velocity at the inlet was generated. The flow velocity increased gradually from 0 to 2.5 m/s and remained constant thereafter. The simulation of the scour process is depicted in Figure 8. To determine the fundamental frequency, the structural displacement in the current direction at the pile top was measured.

As illustrated in Figure 9(a), two free-decay signals occurred at the beginning of the linearly increasing and steady intervals of the flow velocity and were applied to determine the fundamental frequency under different scour conditions. Table 3 presents the frequency comparison under the conditions listed in Table 1. The simulation result

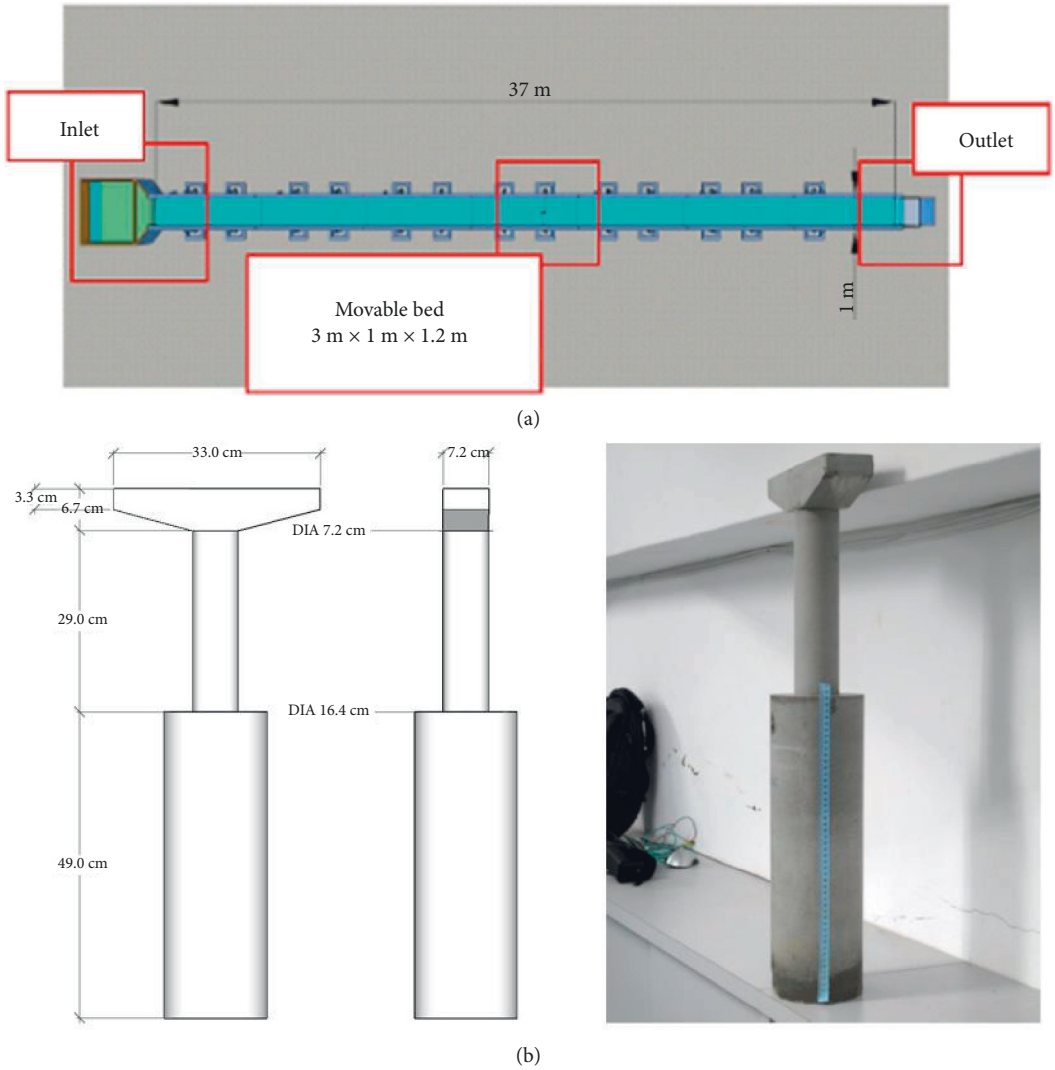


Figure 4: Scour experiment setup. (a) Sink facility. (b) Concrete pier model.

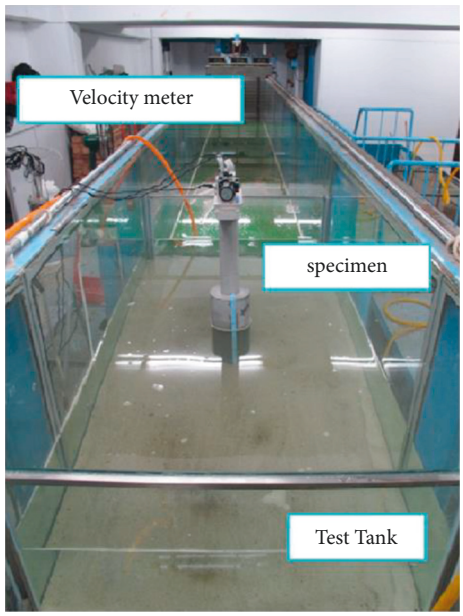


Figure 5: Velocity meters.

is depicted in Figure 9(b). Three different lines present different embedded depths: the blue line is 8 cm, the orange line is 6 cm, and the yellow line is 5 cm. As shown in Table 3, the numerical model exhibited errors of 3.2% and 5.0% in the frequency domain when the embedded depths were 6 cm and 5 cm. The accuracy may be improved by adjusting the size of the element or the boundary condition setting. In general, the scouring phenomenon of the bridge column can be illustrated by the proposed FSI model.

## 4. Practical Application

A practical bridge, the Shi-Bin Bridge, was further considered for scour stability assessment. This bridge is one of the most important bridges in Taiwan, as it connects two major counties by crossing over the Zhuoshui River. To protect the bridge from erosion and scour by the river, it is necessary to investigate the health condition of the structure. Therefore, the Shi-Bin Bridge was selected for scour monitoring.

The Shi-Bin Bridge was built in July 1991. This bridge is 2730 m long, and its clear width is 18 m. The bridge is

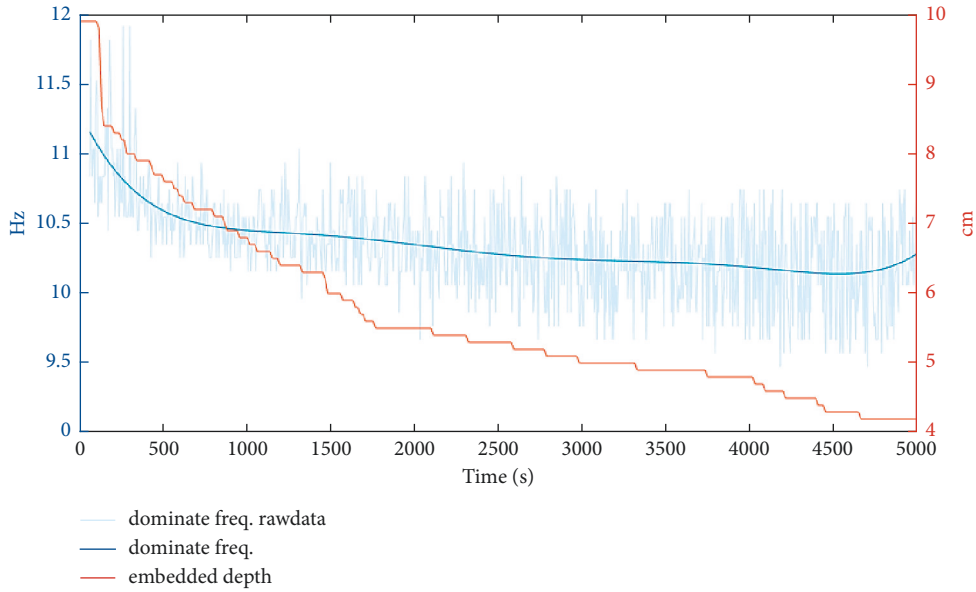


Figure 6: Dominant frequency and corresponding embedded depth.

Table 1: Dominant frequency and embedded depth selected from the scaled scour test.

| Embedded depth (cm) | 8 | 6 | 5 |
|---|---|---|---|
| Dominant frequency (Hz) | 10.76 | 10.41 | 10.21 |
| Water depth (cm) | 10.69 | 10.44 | 10.08 |

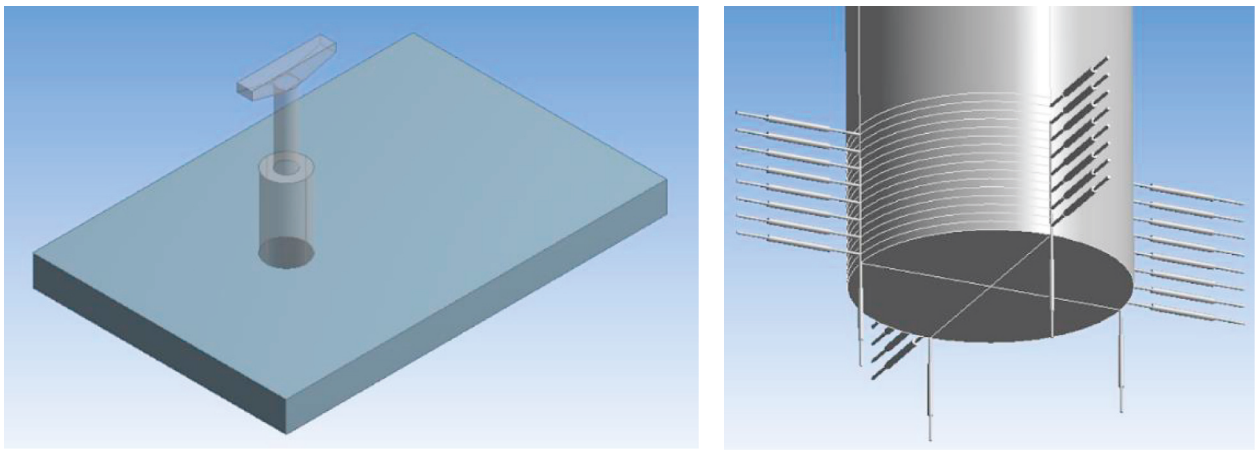

(a) (b)

Figure 7: Numerical model in FSI simulation. (a) Bridge pier and fluid block. (b) Soil springs in the model.

Table 2: $N$ value at each range of the repose angle of soil.

| SPT-N | Density of sand | $\phi$ |
|---|---|---|
| <4 | Very loose | <28 |
| 4–10 | Loose | 28–30 |
| 10–30 | Medium | 30–36 |
| 30–50 | Dense | 36–41 |
| >50 | Very dense | >41 |

composed of 78 spans, and each span is 35 m long. As shown in Figure 10, the Shi-Bin Bridge comprises a four-lane original bridge and a pair of two-lane extension bridges. With a three-column design as the pier, the original four-lane bridge supports decks with seven simply support Precast Concrete-I (PCI) girders. A total of 36 piles in a group are connected to a 2 m thick pile cap, and each pile is 33 m long. For the extension bridge, the single-column pier

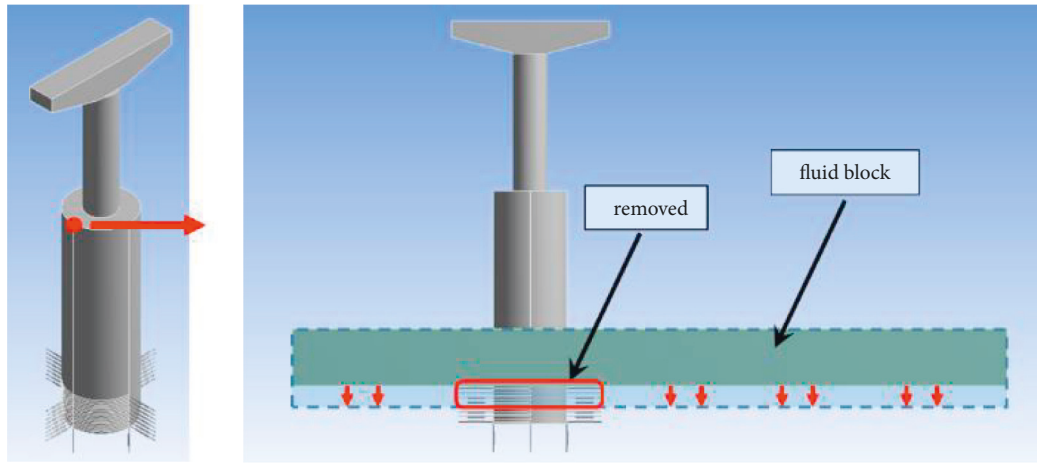


Figure 8: The simulation of the scour process. (a) Pile top displacement. (b) Removal of embedded depth.

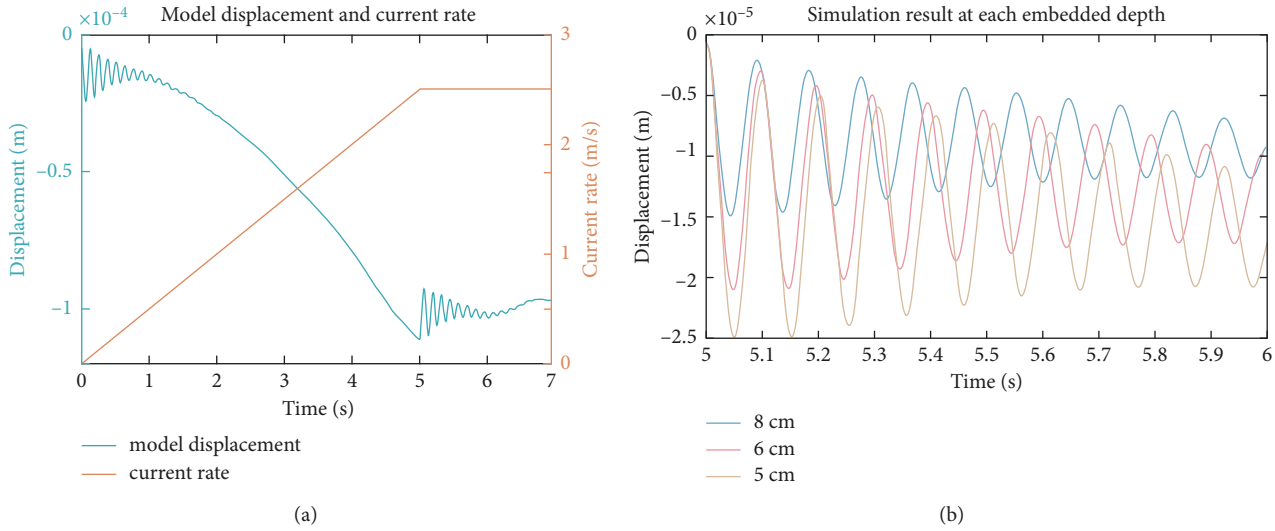


Figure 9: Simulation results of the scour process. (a) Displacement and flow velocity. (b) Comparison under different embedded depths.

Table 3: Frequency comparison between governing variables experiment and simulation.

| Embedded depth (cm) | 8 | 6 | 5 |
|---|---|---|---|
| Freq. (experiment) | 10.76 | 10.41 | 10.21 |
| Freq. (simulation) | 10.77 | 10.07 | 9.70 |
| Error | 0.1% | 3.2% | 5.0% |

supports decks with four simple support PCI girders. A group of 20 piles is connected to a 2 m thick pile cap where each pile is 33 m long.

To decrease the enormous numbers of joints, elements, and degree of freedom to simplify the calculation, only one pier column model was built in this study. However, the mass of this simplified model was less than the practical pier column, which may cause the result of the simulation to be unreliable. To solve this problem, the mass of the pier column and the cap beam were deducted first, and the distributed mass was loaded on the cap beam in the numerical model. After these steps, the mass of the model can reflect the condition of the practical pier column.

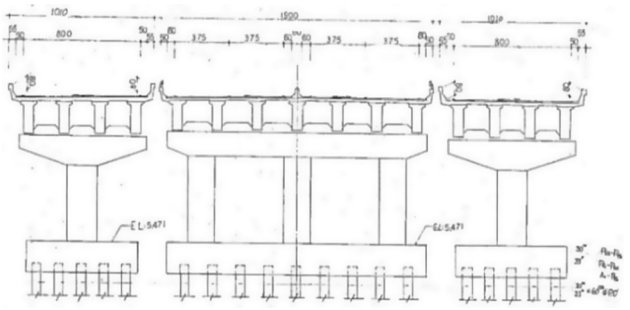

Figure 10: Cross-sectional view of the Shi-Bin Bridge.

According to the as-built drawing, each pier of the extension bridge bears a total weight of 558 tons, including the pier, column, cap, beam, PCI girders, and deck plate. The

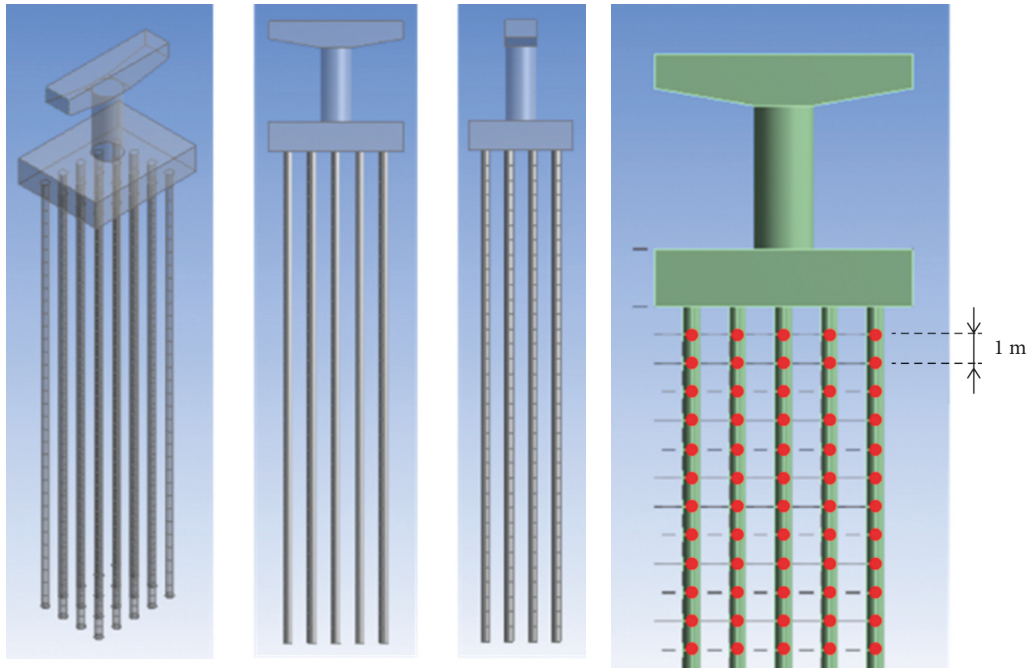


Figure 11: Numerical model of the Shi-Bin Bridge. (a) Column and piles. (b) Arrangement of soil springs.

weights of the deck, PCI girder, and vehicle were transferred through the cap, beam, and column to the foundation of the pier structure. As the compressive strength of the prestressed beams of 350 kgf/cm$^2$ and a unit weight of 2400 kg/m$^3$ was used on the bridge abutments, pier columns, and deck plates, the total mass should be deducted 113 tons by calculation. Thus, the mass of PCI girders and deck, a total of 445 tons per pier, was set at the top of the cap beam.

*4.1. FSI Simulation.* As shown in Figure 11(a), the model of the Shi-Bin Bridge, including the cap, beam, column, pile cap, and pile, was established according to the geometric design of the bridge. To simplify the connection between the pier and piles, the hollow concrete pile of the bridge was replaced by solid concrete piles. Moreover, the soil springs were set in the current direction, driving direction, and under pile. Thus, the stability of this model can be supported by the soil springs.

The model and soil spring stiffness were tuned according to the results obtained from monitoring of ambient vibration at pier 16 and geological prospecting near pier 15. A velocity meter (VSE 15D) was placed at the cap beam of the pier to collect data for the first 5 minutes every hour at a sampling rate of 200 Hz in three directions. The vibration data in the current direction were applied to obtain the dynamic properties of the pier, which involved a fundamental frequency of 2.34 Hz. The $N$ value was set to 25 to define the stiffness of the soil spring in this study. Regarding the setting of soil springs, four soil springs were evenly set in a vertical direction under the foundation. Moreover, in both the longitudinal and transversal directions, the soil springs were set every 1 m in the vertical direction according to the group pile design of the foundation. Thus, the soil springs were placed in an array to enhance stability in the numerical model, as shown in Figure 11(b).

A linearly increasing flow velocity was applied to the inlet boundary condition to avoid simulation failure. Two free-decay signals were observed with the displacement of the pile top along the current direction. To define the structural displacement at the top of the pile under different scour and flow velocity conditions, the mean displacement was calculated as the displacement index in the steady state.

The scour depth, flow velocity, and water level were considered the governing variables of pier stability, and a sensitivity test was conducted to determine the dominant variables. As one of these three variables changed, the other two were kept constant. For example, a variety of displacement could be observed with the scour depth changing continuously, while the flow velocity and water level were constant. Results obtained from a simulation considering a scour depth of 10 m, flow velocity of 0.5 m/s, and elevation of 8.47 m were used as the reference for assessment, as shown in Figure 12. The result of the sensitivity test is shown in Table 4. When the scour depth changed from 10 m to 0 m, the displacement changed from 46.4% to 99.6%. The displacement changed from 116.4% to 401.7% when the flow velocity was variable; however, the displacement changed from 4.8% to 9.5% when the variable was the water level. That is to say, the maximum impact of displacement was investigated when the flow velocity was variable, whereas the minimum influence was found with the change in the water level.

Table 4: Sensitivity test of boundary condition.

| Scour depth (m) | 10 | 8 | 6 | 4 | 2 | 0 |
|---|---|---|---|---|---|---|
| Displacement (m) | **5.83E-04** | 3.12E-04 | 1.18E-04 | 4.24E-05 | 7.94E-06 | 2.30E-06 |
| Sensitivity (%) | — | 46.44 | 79.73 | 92.73 | 98.64 | 99.60 |
| Flow velocity (m/s) | **0.5** | 1 | 1.5 | 2 | | |
| Displacement (m) | **5.83E-04** | 1.26E-03 | 1.88E-03 | 2.92E-03 | | |
| Sensitivity (%) | — | 116.35 | 222.40 | 401.72 | | |
| Water level (m) | **3** | 5 | 1 | | | |
| Displacement (m) | **5.83E-04** | 5.55E-04 | 5.28E-04 | | | |
| Sensitivity (%) | — | 4.75 | 9.47 | | | |

The result of the sensitivity test is shown in Table 4 where the bold values represent the reference for comparison.

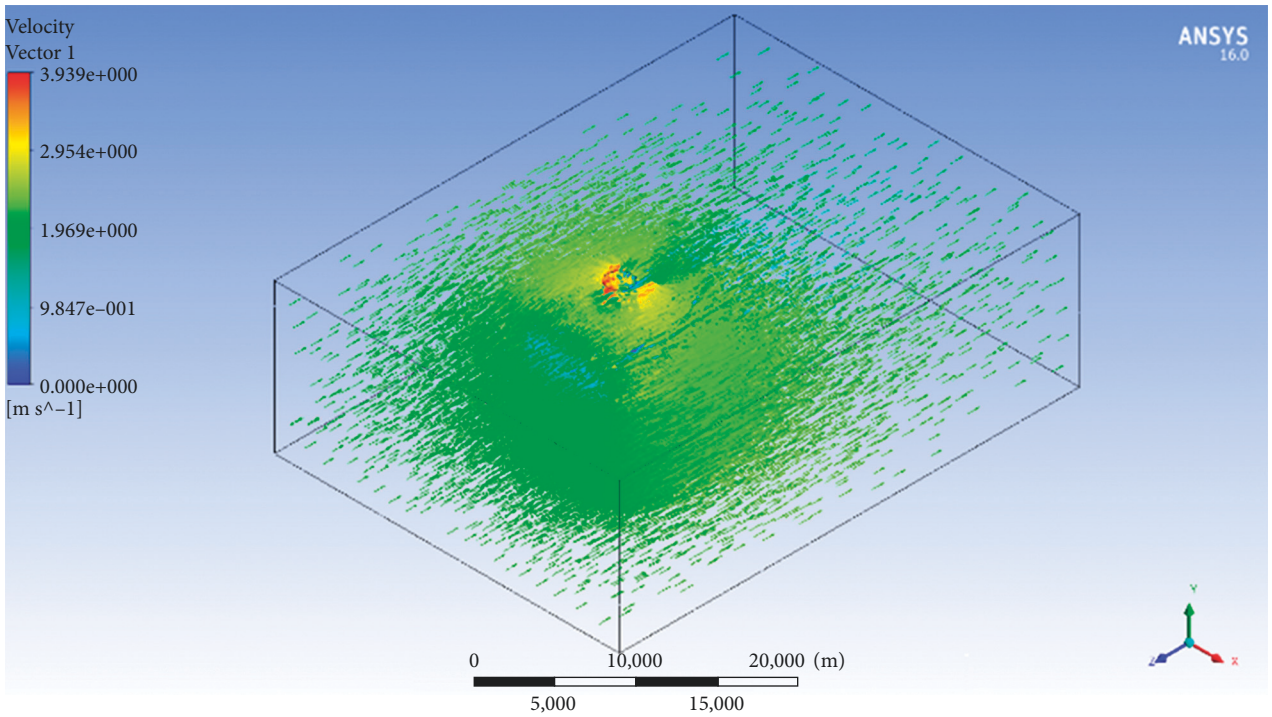


Figure 12: The reference scour scenario for assessment (scour depth of 10 m).

Figure 13 illustrates the structural displacement observed at the top of the pile under different scour conditions. In the FSI simulation, conditions involving a 10 m scour depth could result in simulation failure at a high flow velocity because the deflections of the model were too large. Moreover, two simulation conditions involving flow velocities of 2.5 and 3.0 m/s also led to simulation failure. The displacements of the two conditions were obtained using the extrapolation method with the cubic curve. From the result shown in Figure 13, whether the variable is flow velocity or scour depth, the changing trends are similar. The higher the flow velocity is, the larger the displacement happens. The displacement also increases when the scour depth becomes larger.

The fluid behavior reflecting the downflow, horseshoe vortex, and wake vortex under each boundary condition could be obtained from the simulation results. For the 10 m scour depth and 2 m/s flow velocity, the vertical distribution of the flow velocity at the current section is presented in Figure 14. Downflow was observed at the bottom of the column and near the pile foundation. This flow, which was parallel to gravity, was engendered by the obstacle near the pile cap.

Figure 15 depicts the distribution of the flow velocity at the transversal section. The velocity on the top is about 3.939 m/s, and horseshoe vortices occurring near the bottom of the column can be observed. The horseshoe vortices usually form around obstacles such as the bridge pier in the flowing water. Scouring of the riverbed may be caused by horseshoe vortices from both upstream and downstream of the pier. Meanwhile, the vortices occurring near the pile changed with time and distance from the riverbed, indicating that these vortices could be classified as wake vortices. Although the vortices at the transversal section were not generated from the downflow, the riverbed material near this position was eroded, thus causing scouring.

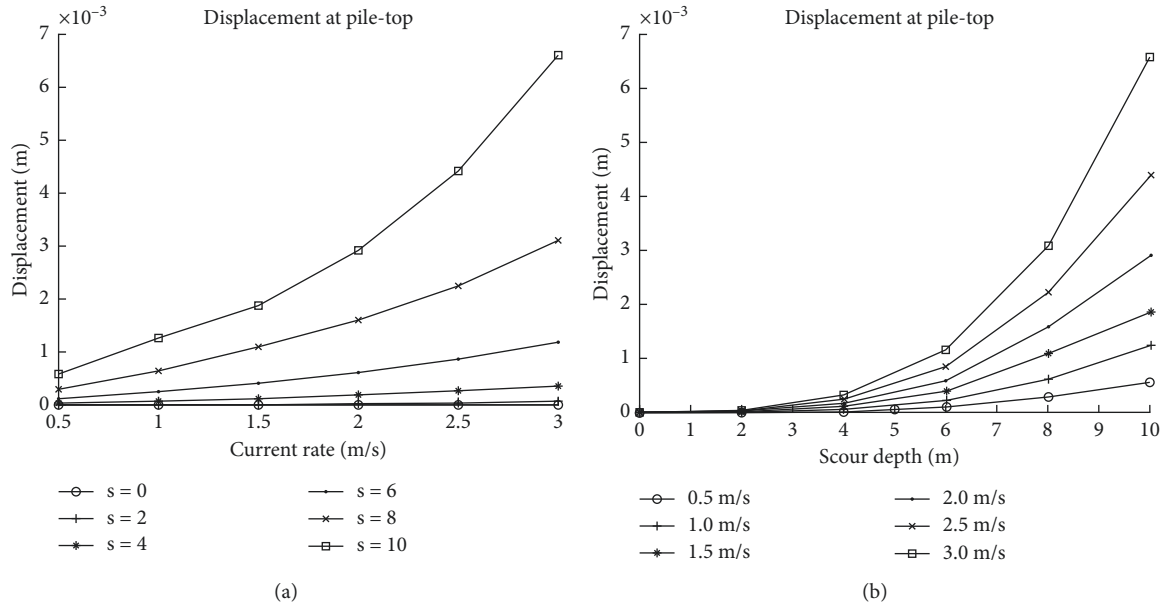


Figure 13: Structural displacement at the pile top under different conditions. (a) Flow velocity. (b) Scour depth.

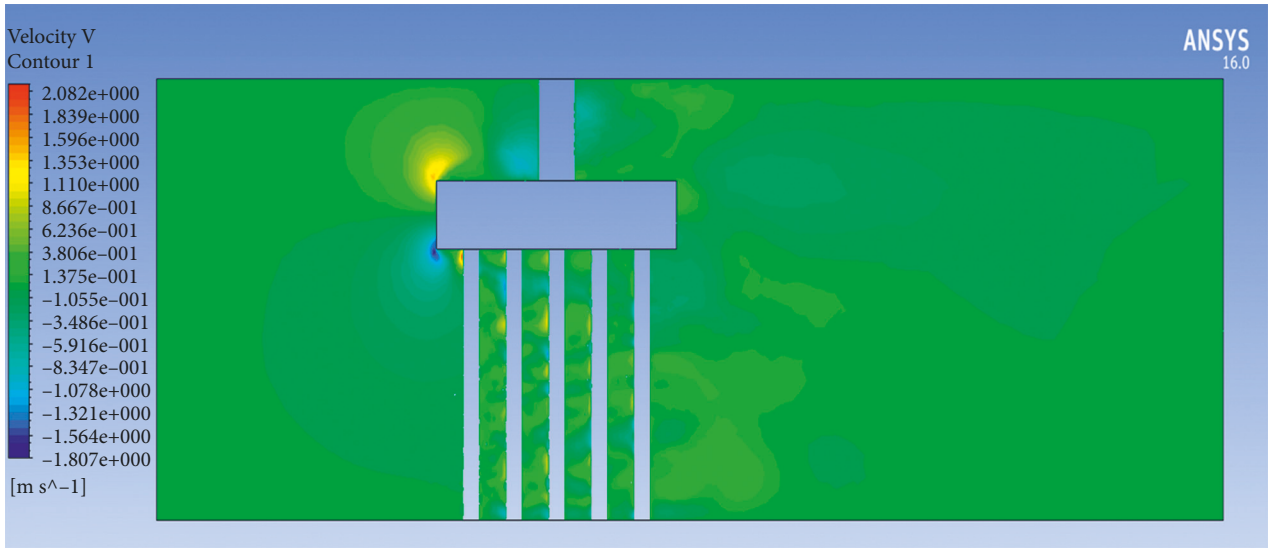


Figure 14: Distribution of vertical flow velocity at the current section.

Figure 16(a) depicts the distribution of the flow velocity at the top. The fluid behavior near the column was stable with no vortex. The smooth flow indicated that no wake vortex or Kármán vortex street occurred near the pier column. However, the Kármán vortex street should occur for a fluid with a Reynolds number of more than 40 [26]. In this study, Reynold's number was more than $1.05 \times 10^6$. Therefore, a 2D simulation of the Shi-Bin Bridge was further conducted, and the Kármán vortex street was observed at the column, as shown in Figure 16(b). The possible reason for the Kármán vortex street not occurring in fluid-solid coupling is that the time interval used in fluid-solid coupling was longer than the period of forming Kármán vortex street.

*4.2. Comparison with Static Loading.* A simulation involving static loading shown in Figure 17 was conducted under the same boundary conditions as the FSI simulation. To simplify the fluid influence, the current force generated by the fluid block in the FSI simulation was replaced by the static external force.

According to the regulation from the Ministry of Transportation and Communications [27], the structural

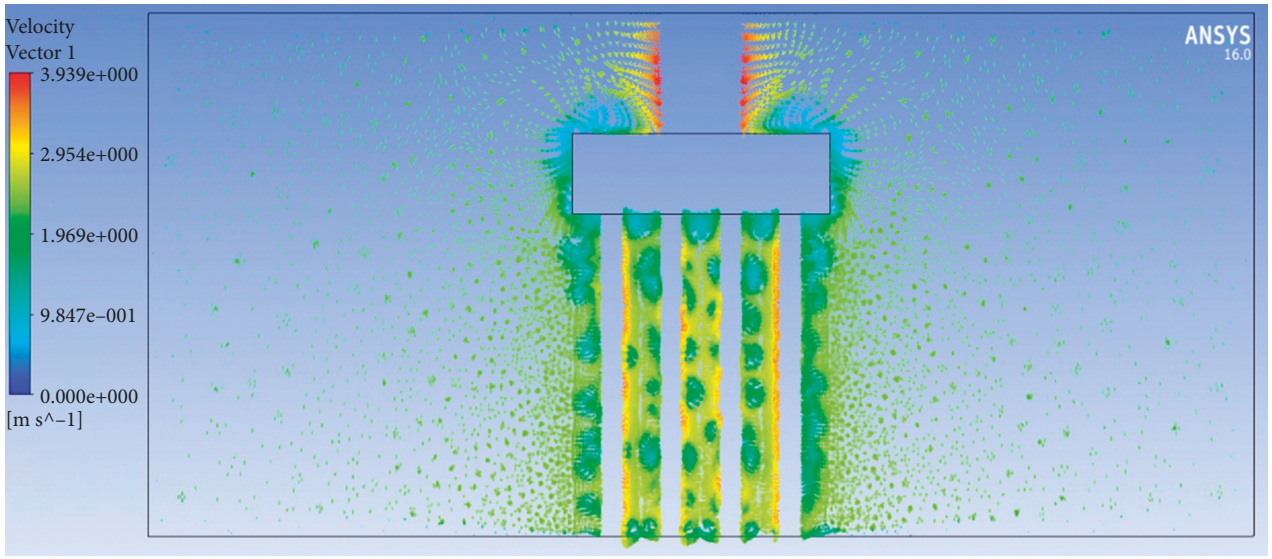


Figure 15: Distribution of flow velocity at the transversal section.

design for RC, PCI, and steel bridges with spans under 150 m should consider the current force defined as

$$P_{avg} = 52.5K\left(V_{avg}\right)^2, \quad P_{max} = 2P_{avg}, \tag{10}$$

where $P_{avg}$, $K$, $V_{avg}$, and $P_{max}$ are the average water pressure, current force constant, average flow velocity, and maximum water pressure, respectively.

The flow velocity was distributed quadratically along the depth direction due to friction at the riverbed. According to the velocity distribution, water pressure was applied linearly to the pile elements, with the maximum pressure occurring at the water surface and a pressure of 0 occurring at the riverbed. $K$ was assumed to be 0.7 and 1.7 at the pile and pier cap, respectively. Through the same boundary conditions as those in the FSI simulation, the displacement at the pile top was determined for various scour depths and flow velocities, as shown in Figure 18.

As depicted, the structural displacements in the FSI simulation were relatively larger than those in the static simulation, and the trends of the structural displacement in the FSI and static simulations were similar. When the flow velocity was assumed to be the governing variable, both results exhibited a slowly increasing slope. According to the comparison, $V_{avg}$ and the current force constant suggested by the code provided a reasonable current force trend; however, the constant value might result in the underestimation of the current force. The results revealed a steeper slope when the scour depth was varied, indicating the importance of the scour depth on the structural behavior.

*4.3. Stability Evaluation.* The FSI simulation, considered a more integrated fluid behavior, indicated a large structural displacement at the pile top. Compared with the pile cap, column, cap beam, and other bridge elements with higher stiffness, the pile of a bridge has a small diameter, which may be a vulnerable characteristic in the bridge structure. In this study, the allowable displacement and ultimate moment of the piles were applied to evaluate the stability of the bridge.

Excessive pile displacement may cause a threat to road users. Furthermore, the $P$–$\Delta$ phenomenon, which can cause column failure, cannot be ignored for pile elements with a slender geometric design. The stability factor [26] of a pile can be defined as

$$Q_s = \frac{P\Delta_0}{VL_c}, \tag{11}$$

where $P$ and $V$ are the axial force and shear force applied to the pile, respectively; $Q_s$, $\Delta_0$, $L_c$, and $M_u$ are the stability factor, relative displacement at the pile top, length of the pile, and ultimate moment of the pile, respectively. According to the mentioned regulation, a stability threshold of 0.25 should be set.

The allowable displacement can then be derived as

$$\Delta_0 = Q_s\frac{Vl_c}{P} = Q_s\frac{M_u}{P}. \tag{12}$$

Therefore, the allowable displacement under a specific axial loading condition can also be defined by examining the ultimate moment of the pile element from a $P$–$M$ interaction diagram.

On the basis of the allowable displacement and ultimate moment, two safety factors, namely, the safety factor based on displacement ($SF_{dis}$) and safety factor based on moment ($SF_{moment}$), are proposed as

$$SF_{dis} = \frac{\Delta_0}{\Delta}, \quad P_{max} = 2P_{avg}, \tag{13}$$

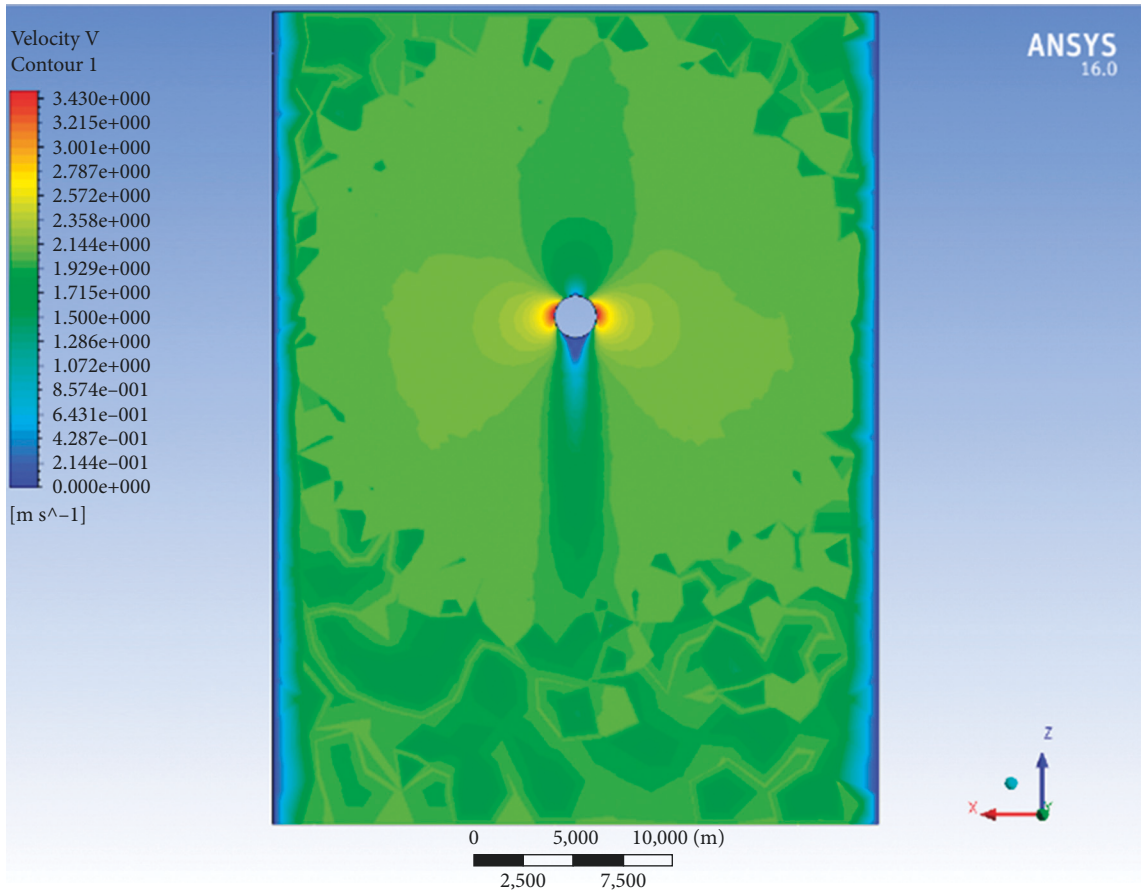


(a)

Figure 16: Continued.

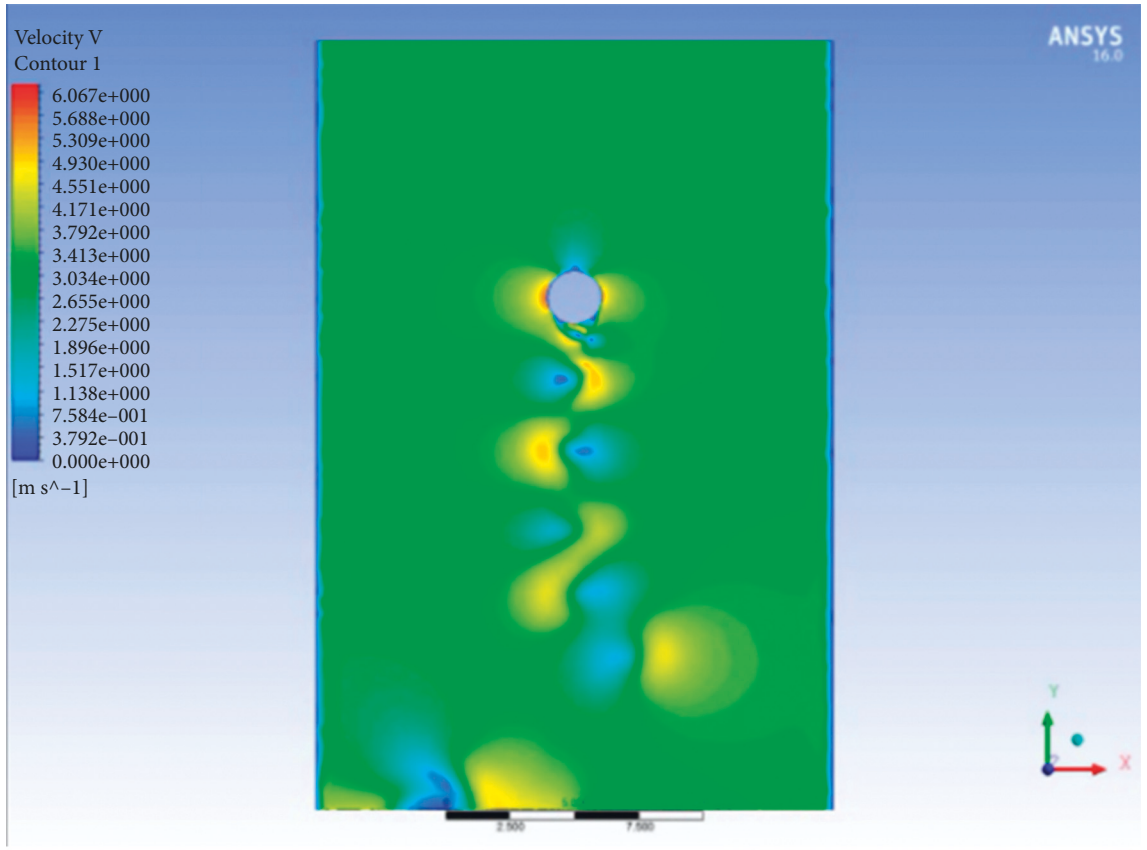


(b)

Figure 16: Top view of the flow velocity. (a) Distribution of the flow velocity. (b) Kármán vortex street in 2D simulation.

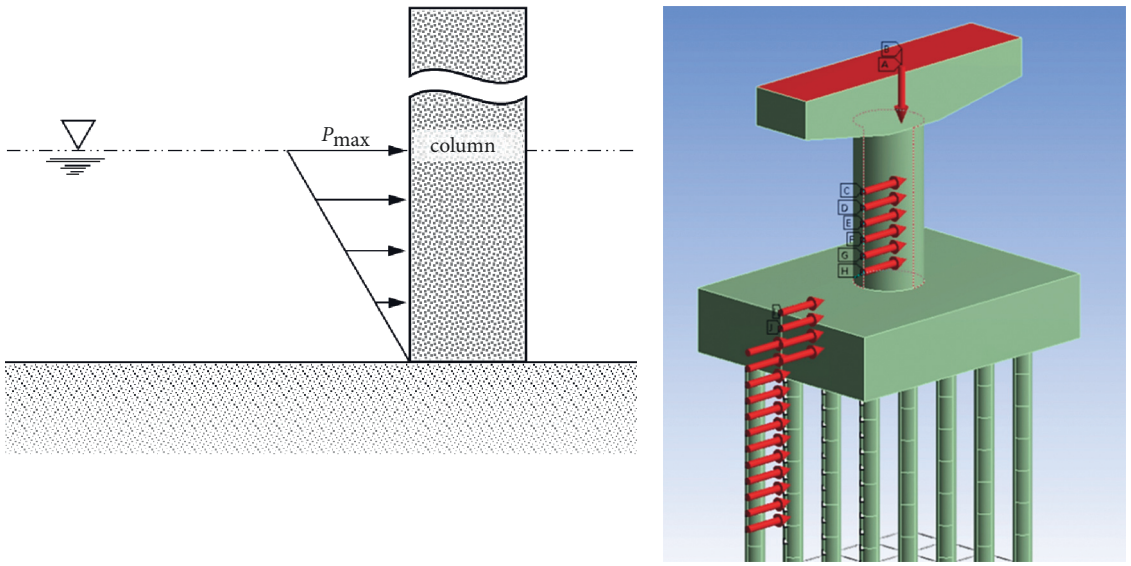


(a) (b)

Figure 17: Static loading simulation. (a) Vertical current pressure distribution. (b) Setting of lateral current force.

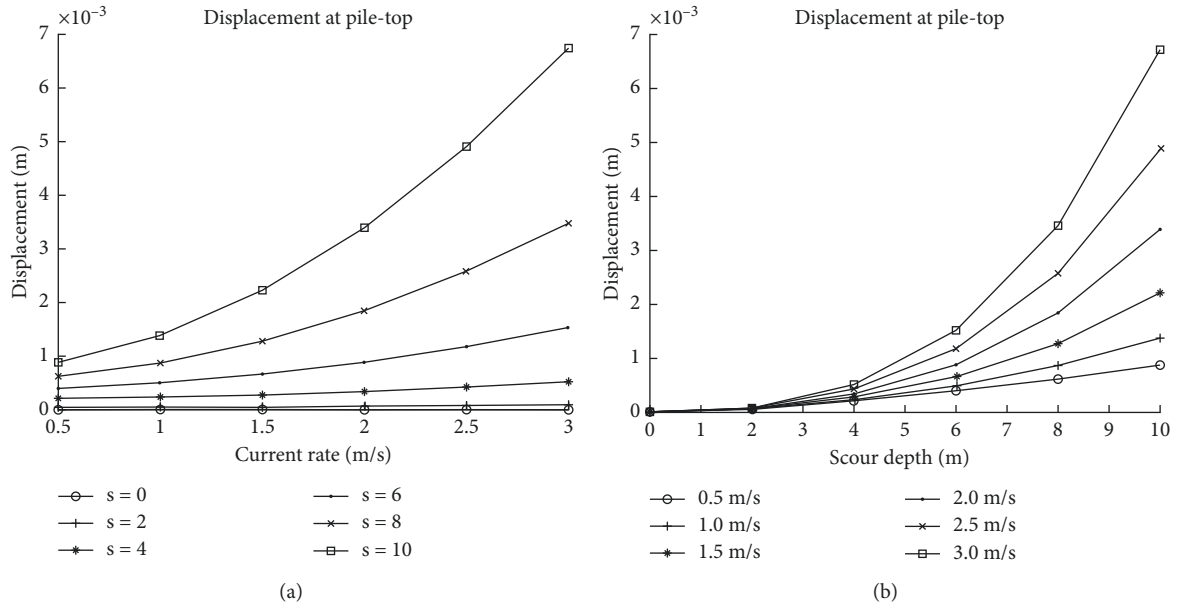


Figure 18: Displacement at the pile top under static loading simulation. (a) Flow velocity. (b) Scour depth.

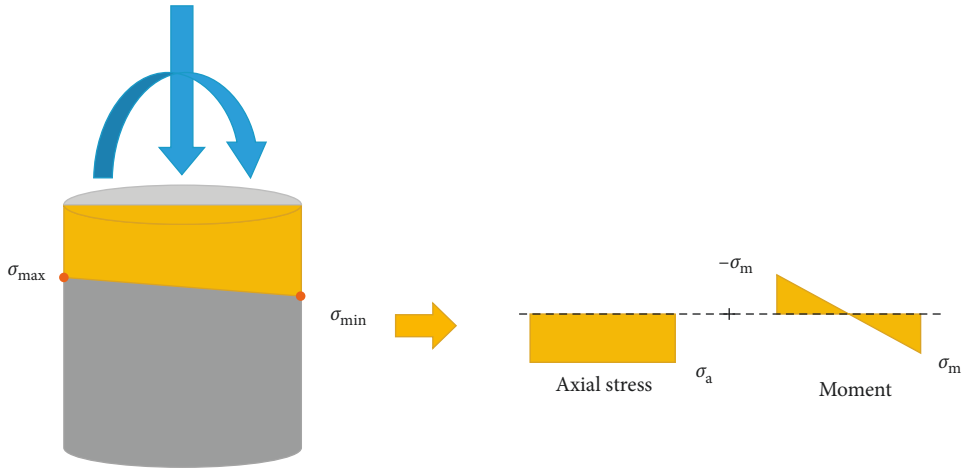


Figure 19: Calculation of the axial force and moment at the pile element.

where Δ and $M$ are the displacement at the pile top and moment at the pile, respectively.

While the structural displacement can be measured directly, the axial force and moment cannot be obtained directly. To obtain the axial force and moment, the stress values of the pile surface at a specific moment were used. Therefore, by calculating the mean value and difference in stress at the upstream and downstream ends shown in Figure 19, the maximum axial force and moment of the pile element can be estimated. Figure 20 shows the simulated axial stress distribution on the pile with the embedded depth of 12 m. The positive maximum axial stress is about 116.54 ton/m$^2$, and the negative maximum axial stress is 117.55 ton/m$^2$. As shown in the figure, the blue color indicates that the minimum axial stress occurs on the soil surface. The stress is increased gradually along the vertical direction to the pile cap, and the maximum axial stress is expressed in yellow color. The stress distribution of the pile was similar to the pressure shown in Figure 17(a), where the force at the water level was the largest and the stress at the bottom was the smallest. The maximum axial forces calculated by different flow velocity and scour depth are shown in Table 5. Among them, the scour depth is calculated based on the elevation of the top of the pile cap being 0 meters. When the scour depths are 0 meters and 2 meters, the top of the pile cap is restricted by soil springs. Thus, the safety factor cannot be calculated according to the relative displacement between the pile top and the riverbed. Therefore, only the axial force value of the erosion depth below 4 meters is listed in Table 5.

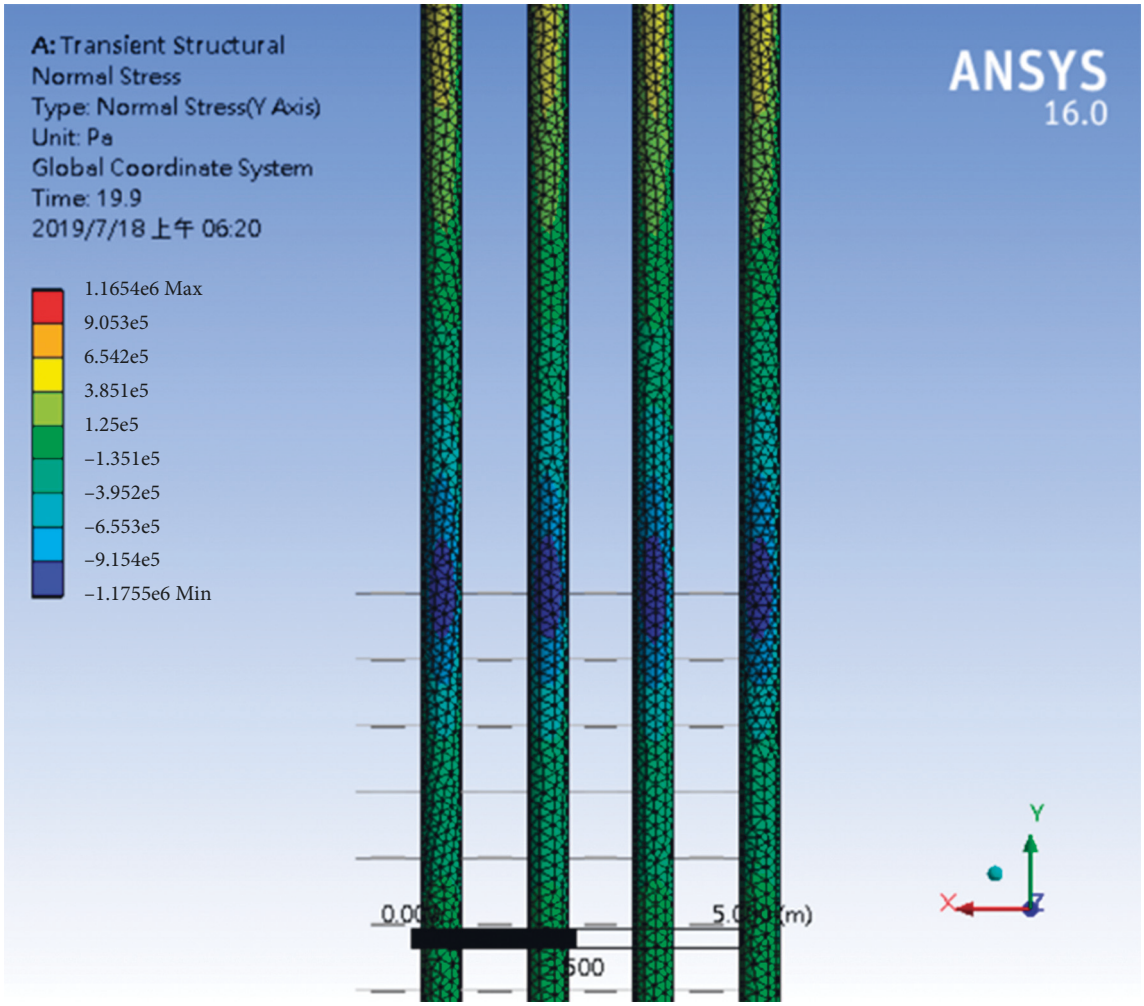


Figure 20: The simulated axial stress distribution on the pile.

Table 5: The maximum axial force of fluid-solid interaction.

| Scour depth (m) | Flow velocity (m/s) | | | | | |
|---|---|---|---|---|---|---|
| | 0.5 | 1.0 | 1.5 | 2.0 | 2.5 | 3.0 |
| 0 | — | — | — | — | — | — |
| 2 | — | — | — | — | — | — |
| 4 | 53413.85 | 53416.30 | 53419.47 | 53384.74 | 53324.93 | 53304.01 |
| 6 | 53927.74 | 53901.52 | 53892.26 | 53828.94 | 53749.19 | 53690.11 |
| 8 | 54856.68 | 54838.10 | 54843.56 | 55132.36 | 54783.61 | 54680.72 |
| 10 | 55701.01 | 55695.67 | 55667.72 | 55629.97 | — | — |

(kgf).

The threshold values of 3 and 2 were set for alert and action decisions, and the derived safety factors are listed in Table 6. The FSI simulation was conducted, and safety factors were obtained as presented in Table 6. The combinations marked in yellow and red represent values lower than 3 and 2, respectively. For example, for the ultimate moment method, the safety factor met the alert threshold when the flow velocity was 3 m/s and the scour depth was 16 m. The action threshold was further triggered when the scour depth reached 18 m. Meanwhile, by considering the allowable displacement method under the same flow velocity of 3 m/s, the safety factors met the alert and action thresholds while the scour depths were 20 m and 22 m, respectively. The result shows that the safety factors are controlled by the ultimate moment. Both methods can provide a rapid and easy method to evaluate the scour stability under extreme events.

Table 6: Safety factors for different scour and flow velocity conditions.

| (a) Allowable displacement method | | | | | | | (b) Ultimate moment method | | | | | | |
|---|---|---|---|---|---|---|---|---|---|---|---|---|---|
| Velocity depth | 0.5 | 1 | 1.5 | 2 | 2.5 | 3 | Velocity depth | 0.5 | 1 | 1.5 | 2 | 2.5 | 3 |
| 0 | — | — | — | — | — | — | 0 | — | — | — | — | — | — |
| 2 | — | — | — | — | — | — | 2 | — | — | — | — | — | — |
| 4 | 5318 | 2825 | 1730 | 1167 | 836.3 | 607.5 | 4 | 996.9 | 1350 | 482.5 | 265.4 | 172 | 118.2 |
| 6 | 1697 | 806.8 | 463.4 | 315.3 | 222.4 | 161.9 | 6 | 554.2 | 220.2 | 116.4 | 74.2 | 51.8 | 37.3 |
| 8 | 592.9 | 283.9 | 165.7 | 113.0 | 80.6 | 58.2 | 8 | 231.4 | 92.8 | 56.8 | 38.5 | 27.1 | 18.5 |
| 10 | 305.3 | 139.8 | 93.4 | 59.9 | 38.6 | 27.9 | 10 | 343 | 68.4 | 43.7 | 26.2 | 14.2 | 9.9 |
| 12 | 172.8 | 76.7 | 48.6 | 31.7 | 20.9 | 15.1 | 12 | 198.4 | 28.8 | 22.1 | 14.7 | 8.7 | 6.0 |
| 14 | 106.2 | 46.0 | 29.5 | 19.1 | 12.4 | 8.9 | 14 | 159.8 | 17.3 | 14.6 | 9.9 | 5.7 | 4.0 |
| 16 | 69.7 | 29.6 | 19.1 | 12.3 | 7.9 | 5.7 | 16 | 132.5 | 11.1 | 10.2 | 7.0 | 4.0 | 2.8 |
| 18 | 48.0 | 20.0 | 13.1 | 8.4 | 5.3 | 3.8 | 18 | 112.3 | 7.5 | 7.4 | 5.2 | 2.9 | 2.0 |
| 20 | 34.4 | 14.1 | 9.3 | 5.9 | 3.7 | 2.7 | 20 | 96.8 | 5.3 | 5.6 | 4.0 | 2.2 | 1.5 |
| 22 | 25.5 | 10.3 | 6.8 | 4.3 | 2.7 | 1.9 | 22 | 84.7 | 3.8 | 4.3 | 3.1 | 1.7 | 1.2 |
| 24 | 19.3 | 7.7 | 5.1 | 3.2 | 2.0 | 1.4 | 24 | 74.9 | 2.8 | 3.4 | 2.5 | 1.3 | 0.9 |
| 26 | 15.0 | 5.9 | 3.9 | 2.5 | 1.5 | 1.1 | 26 | 67.0 | 2.2 | 2.7 | 2.0 | 1.1 | 0.7 |
| 28 | 11.9 | 4.6 | 3.1 | 1.9 | 1.2 | 0.8 | 28 | 60.3 | 1.7 | 2.2 | 1.7 | 0.9 | 0.6 |
| 30 | 9.5 | 3.7 | 2.5 | 1.5 | 0.9 | 0.6 | 30 | 54.8 | 1.3 | 1.9 | 1.4 | 0.7 | 0.5 |

## 5. Summary and Conclusions

This study conducted an FSI simulation to evaluate the scour stability of bridge piers. A feasibility assessment was first conducted to evaluate the applicability of the proposed FSI model; small errors were observed between the scaled pier scour experiment and numerical simulation in the frequency domain, demonstrating the feasibility of the method. The proposed FSI model was subsequently applied to simulate the fluid behavior around a bridge structure subjected to scour. Both FSI and static simulations were implemented under different scour depths and flow velocity conditions, and the structural displacements of the pile top were noted. According to the simulation results, a larger structural displacement was observed in the FSI simulation, indicating that the constant applied in the current force calculation may result in an underestimation of the scour effect. By using the *P–M* interaction diagram of the pile element, two safety factors based on the allowable displacement and ultimate moment were proposed. Finally, the critical scour depth for different flow velocities can be rapidly determined according to the alert and action thresholds. In practical application, the boundary condition setting of the FSI model and the balance between the element size and the time spent on simulation should be carefully considered to ensure the performance of the proposed system. The results can serve as a reference in establishing guidelines for bridge and traffic control for preventing disasters and evacuating people during the occurrence of floods.

## Data Availability

The experimental data used to support the findings of this study are available from the corresponding author upon request.

## Conflicts of Interest

The authors declare that they have no conflicts of interest.

## References

[1] A. M. Shirhole and R. C. Holt, *Planning for a Comprehensive Bridge Safety Program*, Transportation Research Record, Washington DC, 1991.

[2] G. W. Parker, L. Bratton, and D. S. Armstrong, *Stream Stability and Scour Assessments at Bridges in Massachusetts" Report Marlborough*, pp. 97–588, Massachusetts-Rhode Island Water Science Center, China, 1997.

[3] M. Heidarpour, H. Afzalimehr, and E. Izadinia, "Reduction of local scour around bridge pier groups using collars," *International Journal of Sediment Research*, vol. 25, no. 4, pp. 411–422, 2010.

[4] C. Brücker, "Digital-Particle-Image-Velocimetry (DPIV) in a scanning light-sheet: 3D starting flow around a short cylinder," *Experiments in Fluids*, vol. 19, no. 4, pp. 255–263, 1995.

[5] W. H. Graf and I. Istiarto, "Flow pattern in the scour hole around a cylinder," *Journal of Hydraulic Research*, vol. 40, no. 1, pp. 13–20, 2002.

[6] B. Yulistiyanto, Y. Graf, and W. H. Graf, "Flow around A cylinder: shallow-water modeling with diffusion-dispersion," *Journal of Hydraulic Engineering*, vol. 124, no. 4, pp. 419–429, 1998.

[7] R. W. MacCormack, "The Effect of Viscosity in Hypervelocity Impact Cratering," *Aerospace Research Central*, vol. 1, pp. 69–354, 1969.

[8] L. J. Prendergast, D. Hester, K. O'Sullivan, and J. J. O'Sullivan, "An investigation of the changes in the natural frequency of a pile affected by scour," *Journal of Sound and Vibration*, vol. 332, no. 25, pp. 6685–6702, 2013.

[9] L. J. Prendergast, K. Doherty, and P. Doherty, "An investigation into the effect of scour on the natural frequency of an Offshore Wind Turbine," *Ocean Engineering*, vol. 101, pp. 1–11, 2015.

[10] W. C. Tseng, Y. S. Kuo, K. C. Lu, J. W. Chen, C. F. Chen, and R. C. Chen, "Effect of scour on the natural frequency responses of the meteorological mast in the taiwan strait," *Energies*, vol. 11, no. 4, p. 823, 2018.

[11] R. C. Chiroux, W. A. Foster, C. E. Johnson, S. A. Raper, and R. L. Raper, "Three-dimensional finite element analysis of soil interaction with a rigid wheel," *Applied Mathematics and Computation*, vol. 162, no. 2, pp. 707–722, 2005.

[12] J. M. Ting, B. T. Corkum, C. R. Kauffman, and C. Greco, "Discrete numerical model for soil mechanics," *Journal of Geotechnical Engineering*, vol. 115, no. 3, pp. 379–398, 1989.
[13] National Design Specifications in Taiwan, "Design Specifications of Highways and Bridges," *Ministry of Transportation and Communications*, Taipei, Taiwan, 2009.
[14] Y. Z. Wang, Z. W. Yin, D. Jiang, G. Y. Zhang, and X. L. Zhang, "Study of the lubrication performance of water-lubricated journal bearings with CFD and FSI method," *Industrial Lubrication & Tribology*, vol. 68, no. 3, pp. 341–348, 2016.
[15] S. Chitrakar, M. Cervantes, and B. S. Thapa, "Fully coupled FSI analysis of Francis turbines exposed to sediment erosion," *International Journal of Fluid Machinery and Systems*, vol. 7, no. 3, pp. 101–109, 2014.
[16] B. Y. Su, L. Zhong, X. K. Wang et al., "Numerical simulation of patient-specific left ventricular model with both mitral and aortic valves by FSI approach," *Computer Methods and Programs in Biomedicine*, vol. 113, no. 2, pp. 474–482, 2014.
[17] T. S. K. Goud, K. A. Sai, and S. S. Prasad, "Analysis of fluid-structure interaction on an aircraft wing," *International Journal of Engineering and Innovative Technology*, vol. 3, no. 9, pp. 146–152, 2014.
[18] M. HAßLER and K. Schweizerhof, "On the influence of fluid-structure-interaction on the stability of thin-walled shell structures," *International Journal of Structural Stability and Dynamics*, vol. 07, no. 02, pp. 313–335, 2007.
[19] J. Wang, S. C. Li, X. Mao, L. P. Li, S. S. Shi, and Z. Q. Zhou, "The establishment of IB-SEM numerical method and verification of fluid-solid interaction," *Geomechanics and Engineering*, vol. 15, no. 6, pp. 1161–1171, 2018.
[20] K. Q. Lee, A. Abu, N. Kato et al., "Vortex-induced vibration characteristics of a low-mass-ratio flexible cylinder," *Structural Engineering & Mechanics*, vol. 75, no. 5, pp. 621–631, 2020.
[21] T. T. Li, M. L. Duan, W. Liang, and C. An, "A hybrid method for predicting the dynamic response of free-span submarine pipelines," *Ocean Systems Engineering*, vol. 6, no. 4, pp. 363–375, 2016.
[22] Y. Cao and H. C. Chen, "CFD simulation of vortex-induced vibration of free-standing hybrid riser," *Ocean Systems Engineering*, vol. 7, no. 3, pp. 195–223, 2017.
[23] M. Zhao and J. W. Zhou, "Review of seismic studies of liquid storage tanks," *Structural Engineering & Mechanics*, vol. 65, no. 5, pp. 557–572, 2018.
[24] J. M. Kim, S. H. Chang, and C. B. Yun, "Fluid-structure-soil interaction analysis of cylindrical liquid storage tanks subjected to horizontal earthquake loading," *Structural Engineering & Mechanics*, vol. 13, no. 6, pp. 615–638, 2002.
[25] C. F. Zhao, N. A. Mo, and Y. L. Mo, "Seismic fragility analysis of AP1000 SB considering fluid-structure interaction effects," *Structures*, vol. 23, pp. 103–110, 2020.
[26] T. V. Kármán, "Uber den Mechanismus des Widerstandes, den ein bewegter Körper in einer Flüssigkeit erfährt," Nachrichten von der Gesellschaft der Wissenschaften zu Göttingen," vol. 1, pp. 509–517, Mathematisch-Physikalische Klasse, 1911.
[27] National Design Specifications in Taiwan, "Seismic Design Specifications and Commentary of Highways and Bridges," *Ministry of Transportation and Communications*, Taipei, Taiwan, 2009.